Original article

Electrical resistivity, permeability, and normal stiffness of fractured crystalline rocks: Simultaneous laboratory measurements subjected to hydromechanical loading

Kazuki Sawayama[ID]*, Jiei So

Institute for Geothermal Sciences, Kyoto University, Beppu 874-0903, Japan

Abstract:
This study presents the first simultaneous measurements of the hydraulic, electrical, and elastic properties of fractured crystalline rocks under uniaxial loading. To elucidate the fluid-related transport in hydrothermal systems based on geophysical measurements, the correlation between permeability and measurable geophysical properties should be comprehensively understood. However, no study has investigated detailed simultaneous changes in the permeability and electrical resistivity of rough-walled fractures under hydromechanical deformation. Herein, this study simultaneously measured these properties in fractured granite and gabbro samples through laboratory experiments. During hydromechanical loading, normal stress was increased up to 50 MPa while a KCl solution was injected into void space. Resistivity was estimated based on electrical impedance and compared with permeability and fracture-specific stiffness changes under elevated stress. Consequently, increasing stress increased resistivity and stiffness for ~ 1 decade while decreased permeability for ~ 3 decades. The resistivity increase was lower in granite samples than that in the gabbro sample owing to lower matrix resistivity. Based on the measured matrix properties, this study estimated the electric aperture and hydraulic aperture. The ratio of electric aperture to hydraulic aperture decreased with increasing stress, reaching 0.3-0.4 at stress of > 15 MPa. These results suggest that the permeability-resistivity relationship is nonlinear and matrix effect can be insufficient at higher stress such as geothermal reservoirs. Meanwhile, the permeability-stiffness relationship might be controlled primarily by the rock type, while the resistivity-stiffness curves were regulated by the fracture surface state. These different sensitivities suggest that simultaneous measurements of the electrical and elastic properties aid in interpreting permeability changes.

1. Introduction

Fractures are ubiquitous in geological formations and crucial in regulating the crustal fluid behavior. Owing to their higher permeability than intact host rocks, fractures largely influence fluid movement through subsurface systems (Brace, 1980). Therefore, understanding the fracture flow behavior is essential for optimizing natural-resource extraction, geosequestrating carbon or nuclear waste disposal, and effec-tive environmental remediation. In the resource management field, geothermal resources are attracting attention as clean energy sources in decarbonized societies. Typical hydrothermal systems are fracture systems developed in impermeable host rocks (e.g., volcanic rocks, hard pyroclastic rocks, and plutonic rocks). As fractures form the primary migration pathways of geothermal fluids, an accurate characterization of the fracture flow behavior can improve and enable the sustainable extraction of geothermal resources. Moreover, the

development of a monitoring technique for subsurface flow is urgently required for the Enhanced Geothermal System (EGS) project to reduce environmental impact (i.e., induced seismicity) and enhance recovery efficiency.

Although subsurface fluid flow is invisible, geophysical observations have succeeded in identifying subsurface fluids. For instance, the electrical resistivity structure reveals the presence of fluid and enables subsurface permeability estimates in geothermal and hydrothermal areas (Matsunaga and Kanda, 2022; Yamaya et al., 2022). Time-lapse monitoring has detected electrical resistivity changes caused by subsurface stress perturbations associated with EGSs (Peacock et al., 2013; Didana et al., 2017; Johnson et al., 2024). Despite recent advances in geophysical measurement techniques, fracture permeability evaluations based on the geophysical properties are inhibited by a lack of sufficient data on fractured rocks. Meanwhile, changes in permeability caused by variations in subsurface stress may be linked to electrical resistivity, which can be remotely monitored. Models that relate permeability to the electrical resistivity of porous media (Cai et al., 2019; Glover et al., 2006) enable permeability estimates based on the electrical properties (Yamaya et al., 2022). However, such approaches are suitable only for relatively uniform fluid flows in porous media, whereas fluids in fractured rocks preferentially flow through the critical neck of the aperture (Pyrak-Nolte et al., 1988; Nolte et al., 1989). Some field observations have detected unusual changes in the permeability and resistivity of fractured rocks (Park, 1991; Xue et al., 2013), which cannot be explained by experimental findings obtained with intact rocks, demonstrating the important role of macroscopic fractures in the field-scale phenomenon. To date, detailed simultaneous changes in the geophysical properties of fractured rock masses have not been elucidated.

Few studies have investigated the geophysical properties of fractured rock masses. Stesky (1986) measured electrical conductivity (inverse of resistivity) changes in a saw-cut fractured sample under confining pressure and reported that permeability and conductivity are linearly related in a logarithmic coordinate. Conversely, numerical studies based on rough-walled fractures demonstrated a nonlinear relationship between permeability and resistivity (Brown, 1989; Kirkby et al., 2016), resulting from heterogeneous flow distributions (Sawayama et al., 2021a). A pioneering study of simultaneous laboratory measurements of permeability and resistivity under confining pressure was reported by Sawayama et al. (2021b); however, they could not quantify roughness and fracture apertures, necessitating a more detailed understanding of the effect of the surface roughness, rock type, and stress on the permeability-resistivity relationship. Because numerical simulations do not fully capture fracture surface changes under deformation, this study developed an experimental system that simultaneously measures permeability and electrical resistivity during hydromechanical loading to verify whether the permeability-resistivity relationship is linear or nonlinear under actual rock deformation using rough-walled fracture samples.

Based on the developed experimental system, this study simultaneously measured stress-induced changes in permeability, electrical resistivity, and normal stiffness while de-

forming a specimen with a rough-walled single fracture. The hydroelectrical properties depend on the connectivity and tortuosity of flow paths, while the elastic properties relate to fracture asperity contacts. Although all these dependencies are related to the fracture geometry, they are not necessarily mutually correlated and not elucidated under the experimental hydromechanical loading. By simultaneously measuring these properties in identical samples, their similarities and variations under the actual deformation are discussed. Based on such investigations, this study aims to elucidate the relationships between permeability and the geophysical properties of rough-walled fractures. These fundamental findings may help to develop a model that estimates permeability from the geophysical properties.

2. Materials and methods
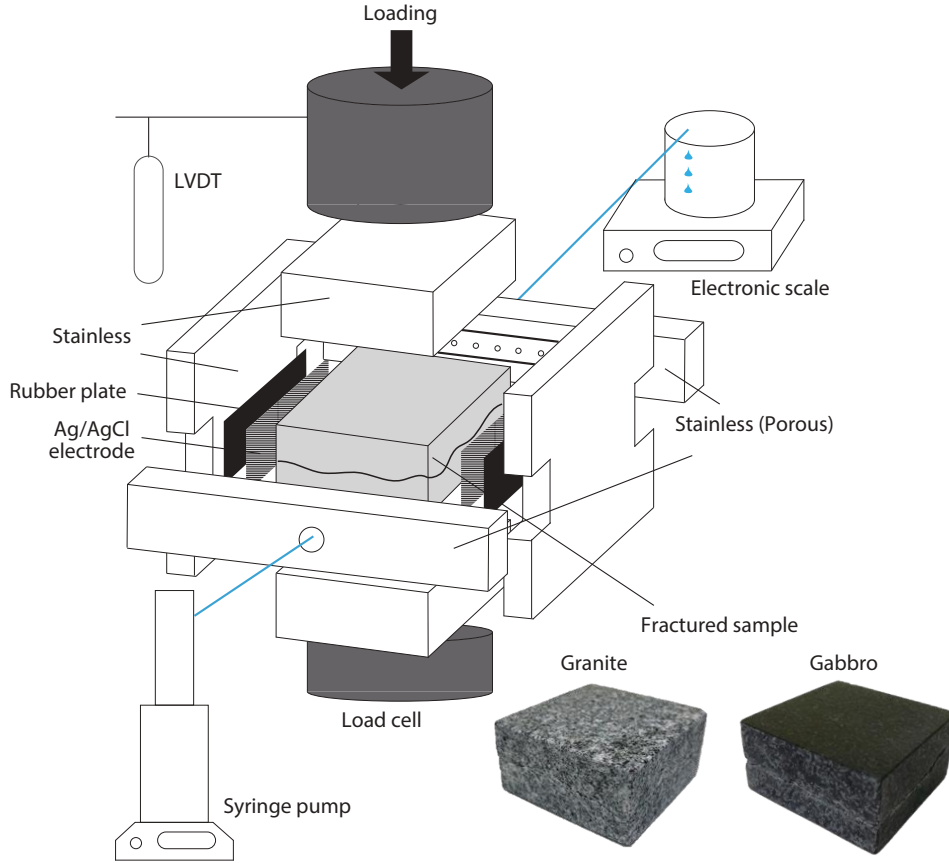
2.1 Experimental design

The authors developed the first experimental system that simultaneously measures the electrical resistivity, permeability, and fracture-specific stiffness of fractured blocks. To achieve simultaneous measurements of these properties under normal stress, hydraulic sealing and electrical insulation were installed in the uniaxial loading system (Fig. 1). Slippage was prevented by a pair of jigs that provided hydraulic sealing and mechanical support, ensuring pure normal deformation. During the uniaxial compression tests, block samples were subjected to an effective normal stress of up to 50 MPa. This covered the stress condition of typical geothermal reservoirs and EGSs (at a depth of ~ 5 km assuming hydrostatic stress and ~ 2 km assuming lithostatic stress in granite lithology). The normal displacements of experimental specimens during deformation were measured using a linear variable differential transformer mounted on a piston. Fluid flow, electrical resistivity, and axial displacement were simultaneously recorded throughout the test.

Flow-through test utilized a pair of stainless steel jigs to prevent water leakage and maintain the differential pore pressure. The jigs for the flow direction contained pores to spread the injected fluid, with the location of the pores adjusted to the fracture plane. The inlet pore pressure was controlled using the ISCO syringe pumps (SyriXus 260X), and the outlet was maintained at ambient pressure. As pore fluid was pumped into the fracture of a jacketed rock sample (0.07-5 MPa), the flow rate of the fluid discharged through the fracture was measured using an electronic balance (atmospheric pressure). From the measured flow rate Q, bulk permeability k in each stress state was calculated using the Darcy's law:

$$\frac{Q}{A} = -\frac{k}{\mu}\nabla P \tag{1}$$

where A, μ, and ∇P denote the cross-sectional area, viscosity, and pressure gradient, respectively.

Resistivity was measured using the electrical impedance method via a four-terminal experimental setup. The electrodes and rubber plates were arranged orthogonal to the flow direction, achieving complete electrical insulation. The current and voltage electrodes were constructed from a silver net ribbon

Fig. 1. Schematic of the experimental design. A LVDT stands for linear variable differential transformer.

with an AgCl-baked coating (Sawayama et al., 2021b). The conductivity of the fluid medium (0.1 mol/L KCl solution) sufficiently surpassed the surface conduction effects within the rock matrix. The electrode-sample contact was enhanced with paper filters soaked in brine water. Electrical impedance Z was given by:

$$Z = |Z| e^{i\theta} = Z' + iZ'' = |Z| \cos\theta + i |Z| \sin\theta \quad (2)$$

where Z' and Z'' denote in-phase (real) and quadrature (imaginary) impedance, respectively, and θ is the phase angle. In this study, the impedance magnitude $|Z|$ and phase angle θ were estimated across a wide frequency spectrum ($10^{-1} - 10^5$ Hz) on an LCR meter (NF, ZM2376). Subsequently, bulk resistivity ρ was determined from the real part of impedance and surface area-to-length ratio A/L as follows:

$$\rho = \frac{A}{L} Z' = \frac{A}{L} |Z| \cos\theta \quad (3)$$

Note that the deformation effect on the sample geometry was corrected using the recorded normal displacement when calculating permeability and resistivity.

2.2 Sample

The experimental samples were granite and gabbroid rocks. The granite sample (Aji granite, Kagawa prefecture, Japan) is fine-grained biotite granite composed mainly of plagioclase, quartz, K-feldspar, and biotite (Watanabe and Higuchi, 2015).

The gabbroid sample (Belfast diabase, Belfast Complex, South Africa) is composed primarily of clinopyroxene and plagioclase (Akamatsu et al., 2019). All samples were sized 60 mm × 60 mm × 30 mm, and tensile fractures were introduced at the sample center (Fig. 1) using a wedge. Each face of blocks was ground with flat-end surfaces parallel to within 0.1 mm. Subsequently, all specimens were rinsed using an ultrasonic cleaner and dried in an oven at 70 °C for at least a day. Then, the fracture surface characteristics and matrix properties were determined prior to experiments.

The fracture topographies of the samples were obtained using an optical profilometer (one-shot three-dimensional measuring macroscope, Keyence, VR-3200) with a 46-μm square-celled grid.

The matrix properties (porosity, electrical resistivity, P-wave velocity, and S-wave velocity) were measured under brine-saturated conditions. The specimens were saturated with the KCl solution (0.1 mol/L) via impregnation, and their porosities were evaluated based on the Archimedes' principle, which determines the suspended weight W_s as the difference between the dry weight W_d and buoyancy. The solid frame volume v_f was then calculated as:

$$\rho_f v_f = W_d - W_s \quad (4)$$

where ρ_f is the fluid density. The void volume v_v was calculated from the difference between the fluid saturated wei-

Table 1. Fracture surface properties of experimental samples. d_{ini}, s, D, and λ denote the initial aperture, surface roughness, fractal dimension, and mismatch wavelength, respectively.

Sample	d_{ini}	Footwall		Hanging wall		λ (mm)
		s (mm)	D	s (mm)	D	
Granite A	0.772	0.930	2.36	0.934	2.42	0.357
Granite B	0.636	1.020	2.28	1.050	2.33	0.353
Gabbro	0.889	0.892	2.37	0.970	2.24	1.65

ght W_f and dry weight as follows:

$$v_v = \frac{W_f - W_d}{\rho_f} \tag{5}$$

From these densities, porosity ϕ was estimated as:

$$\phi = \frac{v_v}{v_v + v_f} \tag{6}$$

Acoustic measurements were conducted via the pulse transmission method using Olympus ultrasonic transducers (V103-RM and V153-RM for P-wave and S-wave velocity measurements, respectively) arranged as a transmitter-receiver pair. Based on the resonant frequency of the transducers, the frequency and amplitude of the input pulse were set to 1 MHz and 10 Vp-p, respectively, using a function generator (NF, WF1974). To improve the signal-to-noise ratio, the transmitted waveforms were amplified using a preamp (NF, 9913) and stacked more than 2,000 times. The first arrival times of the P-wave and S-wave were analyzed from the waveforms recorded by an oscilloscope (Yokogawa, DLM5034) using the Akaike Information Criterion (AIC), where the global minimum of the AIC function corresponds to the onset time of a signal. The AIC criterion requires an appropriate time window, including the waveform regions of interest (Akamatsu et al., 2023). Matrix resistivity was measured as described in Section 2.1.

After these measurements, the samples were restored to their original configuration, jacked by a heat-shrinkable tube and placed in the uniaxial testing frame. Fluid flow, electrical impedance, and normal displacement were simultaneously measured as stress was raised to 50 MPa.

3. Results

3.1 Fracture characteristics and matrix properties

Prior to rock deformation experiments, the fracture characteristics and matrix properties were evaluated. The fractal characteristics of each sample fracture were identified on the mapped fracture surfaces located at the sample center (Figs. 2(a)-2(c)). The initial aperture distributions (Figs. 2(d)-2(f)) were determined by numerically moving the footwall and hanging wall (Figs. 2(g)-2(i)) until they contacted at a single point. Prior to numerical mating, the slope and horizontal offset of fracture surfaces were corrected to minimize the resultant mean aperture. Figs. 2(j)-2(l) show the surface height

histograms of the footwall. The surface roughness value s was calculated as the root-mean-square heights of fracture surface topographies; namely, the standard deviation of the surface height. Granite A and gabbro show similar sharp trend, whereas the histogram of granite B exhibits relatively broader distribution. Overall, the surface height histograms of natural fractures agree with the normal distribution (red curve in Figs. 2(j)-2(l)). Figs. 2(m)-2(o) depict the Power Spectrum Densities (PSDs) of the footwall, hanging wall, and initial aperture profiles. From the PSD slopes of the footwall and hanging wall, the fractal dimension D was determined as:

$$D = 7 - 2b \tag{7}$$

where b is the PSD slope of the surface height (dashed lines in Figs. 2(m)-2(o)). Dotted line in Figs. 2(m)-2(o) denotes the mismatch length scale λ_c determined as the curvature of the PSD of the ratio of the surface height to the initial aperture. At wavelengths below the threshold wavelength, the PSD ratio begins to decrease with decreasing spatial frequency (Matsuki et al., 2006). The analyzed results are summarized in Table 1. Granite A and gabbro exhibited similar roughness and fractal dimension, whereas Granite B had higher surface roughness value and lower fractal dimension. Furthermore, granite and gabbro demonstrated different mismatch length scales. Overall, the results suggest that fractures tested in this study are an acceptable substitute for natural rock fractures (Brown, 1989; Sawayama et al., 2021b).

As results of matrix properties, the porosities, electrical resistivities, and P- and S-wave velocities of the samples are listed in Table 2. The granite samples exhibited higher porosities and lower electrical resistivities and P-wave and S-wave velocities than the gabbro sample.

Variations in the P- and S-wave velocities could be described in terms of the crack density parameter and crack aspect ratio, where their summation represents crack porosity. Meanwhile, resistivity is a function of porosity and crack connectivity. Therefore, by measuring these properties, we could further explore the microstructural characteristics of the pore space of matrices. Following Akamatsu et al. (2023), this study jointly inverted the measured velocities, resistivities, and porosities to determine the crack density parameter, crack aspect ratio, and crack connectivity.

Assuming that composites containing penny-shaped cracks are saturated with water and randomly oriented and do not interact with each other, effective bulk modulus K^* and shear modulus G^* are given by (Kachanov, 1993):
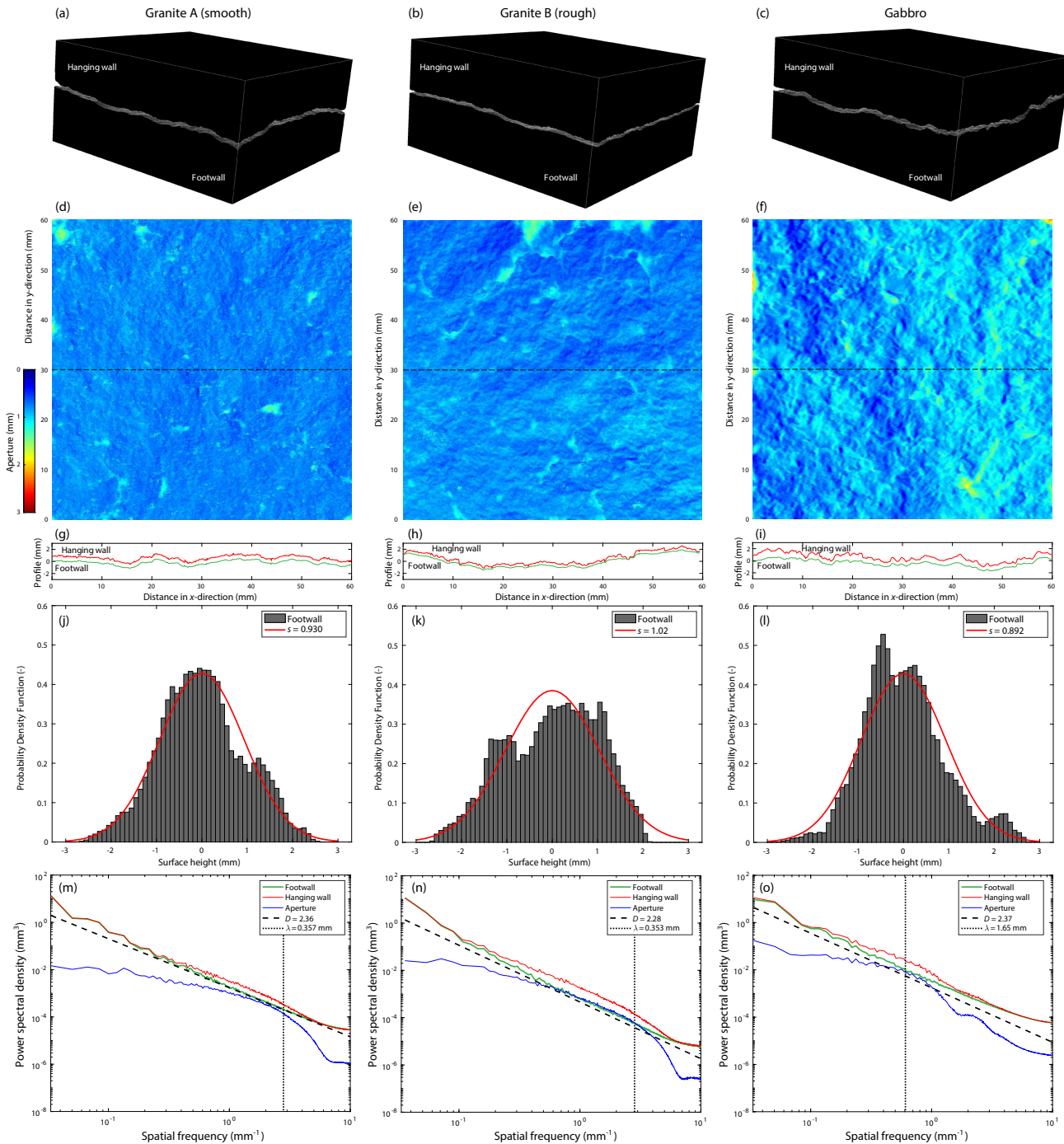
$$\frac{K_0}{K^*} = 1 + \frac{h\varepsilon}{1 - 2v_0}\left\{1 + \left[\left(1 - \frac{v_0}{2}\right)\frac{\delta}{1+\delta} - 1\right]\right\} \tag{8a}$$

$$\frac{G_0}{G^*} = 1 + \frac{h\varepsilon}{1 + v_0}\left\{1 + \frac{2}{5}\left[\left(1 - \frac{v_0}{2}\right)\frac{\delta}{1+\delta} - 1\right]\right\} \tag{8b}$$

$$h = \frac{16(1 - v_0^2)}{9\left(1 - \frac{v_0}{2}\right)} \tag{8c}$$

$$\delta_f = \frac{9\pi(1 - 2v_0)}{16(1 - v_0^2)}\frac{K_0}{K_f}\xi \tag{8d}$$

where v_0 is the Poisson's ratio, ξ is the mean aspect ratio of

Fig. 2. Fractal characteristics of samples: (a)-(c) Three-dimensional layout of the sample, (d)-(f) initial aperture distribution, (g)-(i) cross-sectional profiles of the footwall and hanging wall, (j)-(l) probability density function of the surface height of the footwall, and (m-o) power spectral densities of the footwall, hanging wall, and initial aperture versus spatial frequency (or wavenumber). Dashed line in (d)-(f) represents the location of the cross-section in (g)-(i). s in (j)-(l) denotes the root mean square of the surface height. D and λ in (m)-(o) indicate the fractal dimension and mismatch wavelength dividing the mated and unmated spectral regions, respectively.

Table 2. Summary of the matrix properties of experimental samples.

Sample		ϕ_m (%)	$\log_{10}\rho_m$ (Ωm)	V_p (km/s)	V_s (km/s)	V_p/V_s
Granite A	Footwall	1.41	3.29	5.21	2.91	1.79
	Hanging wall	1.39	3.08	5.31	3.11	1.71
Granite B	Footwall	0.963	3.08	5.54	3.14	1.77
	Hanging wall	1.07	3.18	5.37	3.26	1.65
Gabbro	Footwall	0.647	4.46	6.63	3.54	1.87
	Hanging wall	0.633	4.53	6.57	3.73	1.76

Notes: ϕ_m, ρ_m, V_p, and V_s denote matrix porosity, matrix resistivity, P-wave velocity, and S-wave velocity, respectively.

Table 3. Summary of the inversion results of pore microstructures.

Sample		ε	ξ	f
Granite A	Footwall	0.965	0.00525	1
	Hanging wall	0.748	0.00669	1
Granite B	Footwall	0.708	0.00437	1
	Hanging wall	0.592	0.00956	1
Gabbro	Footwall	0.154	0.00294	0.0790
	Hanging wall	0.147	0.00573	0.0347

Notes: ε, ξ, and f denote the crack density parameter, mean aspect ratio of a crack, and crack connectivity index, respectively.

Fig. 3. Displacement-stress curves of rock samples. Colored circles represent the raw data, and red solid lines denote the fitted results.

cracks, K_f is the fluid bulk modulus (2.25 GPa in our case), and K_0 and G_0 denote bulk and shear moduli of a crack-free material (Fortin et al., 2007). h is a factor describing the penny-shaped geometry and δ_f characterizes the coupling between the stress and the fluid pressure for a given ξ (Guéguen and Sarout, 2009). The crack density parameter ε is defined as (O'Connell and Budiansky, 1974):

$$\varepsilon = \frac{1}{v}\sum c^3 \qquad (9)$$

where c is the radius of a crack and v is the bulk volume. Additionally, this study employed the differential effective medium scheme of Eq. (8) to minimize the effect of interactions between each crack.
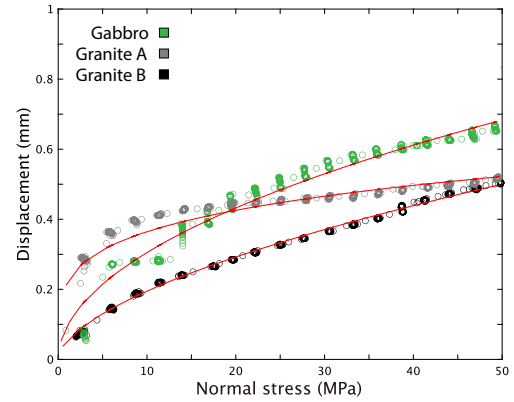
Effective resistivity ρ_{eff} in the same problem could be expressed based on the percolation theory (Guéguen and Dienes, 1989):

$$\rho_{\text{eff}} = \frac{4\rho_f}{f\phi_c} \qquad (10)$$

Crack porosity ϕ_c could be estimated from the crack density and mean aspect ratio as (Kachanov, 1993):

$$\phi_c = \frac{4}{3}\pi\varepsilon\xi \qquad (11)$$

The crack connectivity index f, representing the fraction

of connected paths, could be calculated using the percolation theory based on the Bethe lattice with a coordination number of four (Guéguen and Palciauskas, 1994):

$$f = 1 - 4\left(\sqrt{\frac{1}{p}-\frac{3}{4}}-\frac{1}{2}\right)^3 + 3\left(\sqrt{\frac{1}{p}-\frac{3}{4}}-\frac{1}{2}\right)^4 \qquad (12a)$$

$$p = \frac{\pi^2}{4}\varepsilon \qquad (12b)$$

Based on these equations, electrical resistivity and seismic velocity could be expressed as functions of the crack density and aspect ratio.

Joint inversion calculation revealed that granite had a higher crack density than gabbro, although they had a similar crack aspect ratio (Table 3). Meanwhile, the connectivity index demonstrated fully connected cracks in granite but partially connected cracks in gabbro. These differences affected the bulk properties of these rocks, as discussed later.

3.2 Mechanical property

Fig. 3 depicts the displacement-stress curves of the samples. To reveal net changes in normal displacement caused by fracture closure alone, the displacement data were corrected by subtracting the initial displacement and expected deformation in a rock matrix based on the Young's modulus (60 GPa for
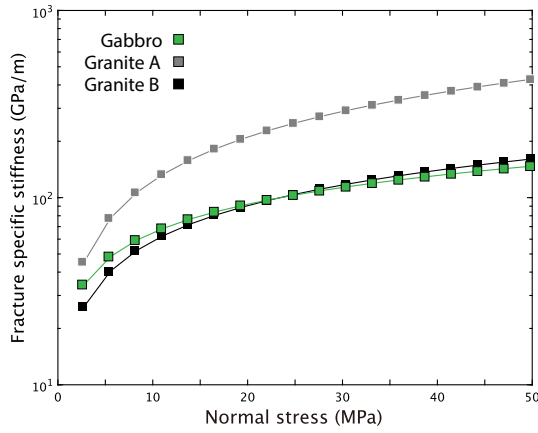
Fig. 4. Fracture-specific stiffness versus normal stress in gabbro (green) and granite (black and gray) rock samples.
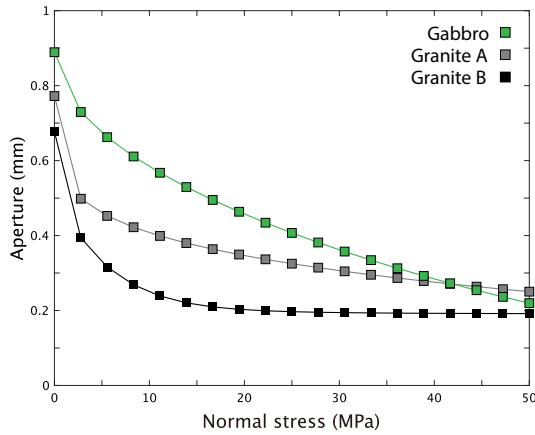

Fig. 5. Mean apertures of gabbro (green) and granite (black and gray) samples versus normal stress.

granite and 100 GPa for gabbro; Akamatsu et al., 2019). Here, this study used the data of the first loading cycle to focus on the simplest loading condition when two surfaces make contact (Pyrak-Nolte and Morris, 2000). Additional unloading and loading to a fracture could induce time-dependent effects with long time constants that were not considered in experiments (Guyer and Johnson, 1999; Pyrak-Nolte and Morris, 2000). Consequently, all samples showed a power-law relationship between stress σ and displacement δ, as previously reported (Goodman, 1976). Assuming the Goodman's empirical power-law relationship, the data was fitted to the following equation:

$$\delta = a_1 \times \left[1 - \exp\left(-\frac{\sigma^{a_3}}{a_2} \right) \right]^{a_4} \tag{13}$$

where a_1, a_2, a_3, and a_4 are empirically coefficients. The curve-fitting results demonstrated that the empirical relationship could capture our experimental data. The fracture-specific stiffness was then obtained by differentiating Eq. (13).

Fig. 4 plots the calculated fracture-specific stiffness as a function of stress. In both rock types, stiffness largely increased with stress under low-stress conditions (~ 15 MPa) and almost saturated under high-stress conditions. A similar nonlinear trend was reported for granite fractures, which might
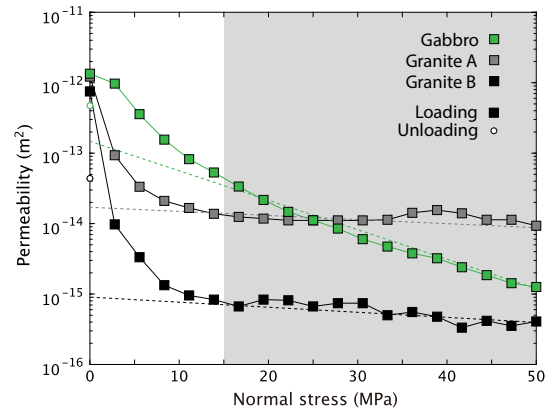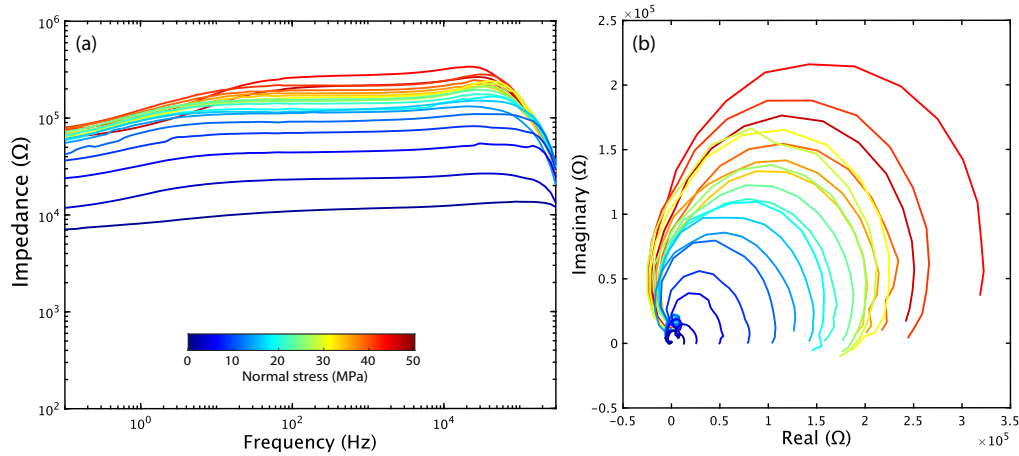

Fig. 6. Permeabilities of gabbro (green) and granite (black and white) versus normal stress. Square plots denote measurements under loading, and circle plots represent those after loading. The dashed lines denote the baseline referring to the data at > 15 MPa of normal stress.

be because a fractured rock tended to behave elastically until fracture eventually closes completely (Pyrak-Nolte and Morris, 2000; Raven and Gale, 1985; Tsang and Witherspoon, 1981). Small discrepancies among the samples might be arising from the fracture surface condition. Based on the similar results obtained for gabbro and granite, stiffness was less affected by the rock type than by the fracture surface roughness. A previous study highlighted that the fracture deformation process is more sensitive to roughness and is primarily controlled by the growth rate of new contact asperities (Pyrak-Nolte and Morris, 2000; Wang and Cardenas, 2016).

Aperture changes could be estimated from the normal displacement, where the initial aperture was estimated from the fracture surface profiles (Fig. 2). Fig. 5 plots the mean apertures of the samples as functions of normal stress. The apertures of all samples monotonically decreased with stress, while the closure rate was moderate under high-stress conditions (Hofmann et al., 2016). Although different rock types exhibited similar trends, they depended on the fracture surface roughness conditions, which might be due to the growth rate of new contact asperities.

3.3 Permeability

Fig. 6 shows the permeabilities of the samples as functions of normal stress. The initial permeabilities of the three samples were quite similar ($\sim 10^{-12}$ m^2), likely because their initial apertures were similar (Fig. 5). However, the permeability trends against stress depended on the fracture surface roughness and rock type. Granite permeability decreased and almost saturated under ~ 15 MPa normal stress, as previously reported in numerous studies (Tsang and Witherspoon, 1981; Raven and Gale, 1985; Sawayama et al., 2021a). The saturation of the permeability change could be related to inelastic deformations, such as the asperity degradation or pressure solution of the aperture (Yasuhara et al., 2004; Hofmann et al., 2016), although our jig prevented any sliding on the fracture surface. The reduction in permeability observed after loading ($\sim$ one order of magnitude) also supported the prese-

Fig. 7. Stress-induced changes in the (a) bode plots and (b) cole-cole plots of gabbro sample.
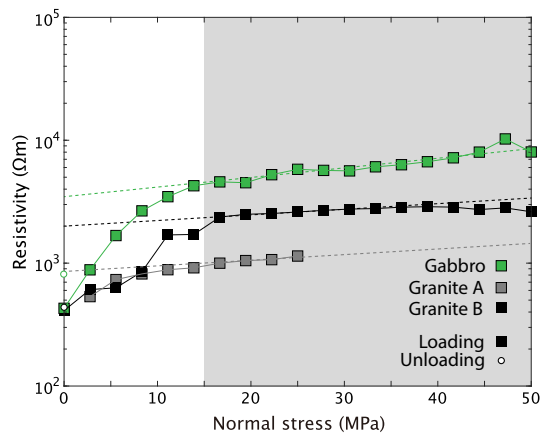
Fig. 8. Resistivities of gabbro (green) and granite (black and gray) versus normal stress. Square plots denote measurements under loading and circle plots represent those after loading. The dashed lines denote the baseline referring to the data at > 15 MPa of normal stress.

nce of inelastic deformation during experiments. The different absolute permeabilities of the granite samples might reflect various aperture and contact states generated owing to their different fracture surface conditions. The permeability of the gabbro sample monotonically decreased with stress. Although the permeability of fractured gabbro has not been previously reported, the measured permeability of a mafic rock continuously decreases until confining pressure reaches ~ 80 MPa (Durham, 1997; Nara et al., 2011). The permeability reduction after loading was not so significant in the gabbro sample, suggesting that inelastic deformation in the sample is smaller than that in granite. Therefore, the discrepant permeability trends of granite and gabbro might be related to different onsets of inelastic deformation (i.e., asperity degradation or pressure solutions) in rocks owing to their different matrix mineral compositions.

3.4 Electrical property

Fig. 7(a) illustrates the representative Bode plots obtained for the gabbro sample under increasing normal stress. Overall, the impedance spectrum exhibited plateau at low frequencies

owing to the resistive component of the sample. Increasing stress gradually decreased the magnitude of impedance. In general, the electrical impedance of rocks contains resistive and capacitive components. In a simple *RC* parallel circuit, where *R* is resistance and *C* is capacitance, complex impedance *Z* in the angular frequency ω domain is determined as:

$$Z(\omega) = \frac{R}{1+(RC\omega)^2} - i\frac{R^2C\omega}{1+(RC\omega)^2} \quad (14)$$

Combining Eqs. (2) and (14), we obtained:

$$\left(Z' - \frac{R}{2}\right)^2 + (Z'')^2 = \left(\frac{R}{2}\right)^2 \quad (15)$$

demonstrating that a plot of Z' versus Z'' on a complex plane forms a semicircular arc (i.e., Cole-Cole circle) that starts from the zero point and centers approximately on the real axis. Fig. 7(b) shows the representative Cole-Cole plots obtained for the gabbro sample under increasing normal stress. The plots were circular, indicating that our measurement system can be expressed as an ideal *RC* parallel circuit. The circle diameter (representing resistance) considerably decreased with increasing stress. Meanwhile, the distance between zero and the starting point of the Cole-Cole circle along the *x* axis (i.e., the left edge), which denotes contact resistance, was nearly zero in our measurement system. The right edge of the Cole-Cole circle represents the critical frequency above which electrode polarization occurs (Liu et al., 2015). The plots suggest the robustness of our measurement system, with negligible contact resistance in our Ag-AgCl electrodes and polarization at frequencies below 12 kHz. The previous study reported the critical frequency of ~ 25 kHz when measuring the electrical impedance of Berea sandstone using Pt and carbon nanotube electrodes (Liu et al., 2015). The difference in critical frequency with our study may be due to the different measurement system. Note that the critical frequency is almost constant in our measurements, which has an insignificant effect on the calculated resistivity trends.

Based on these findings, resistivity was calculated from impedance at 12 kHz. Fig. 8 plots resistivity against normal stress. The initial resistivity values were similar in each samp-
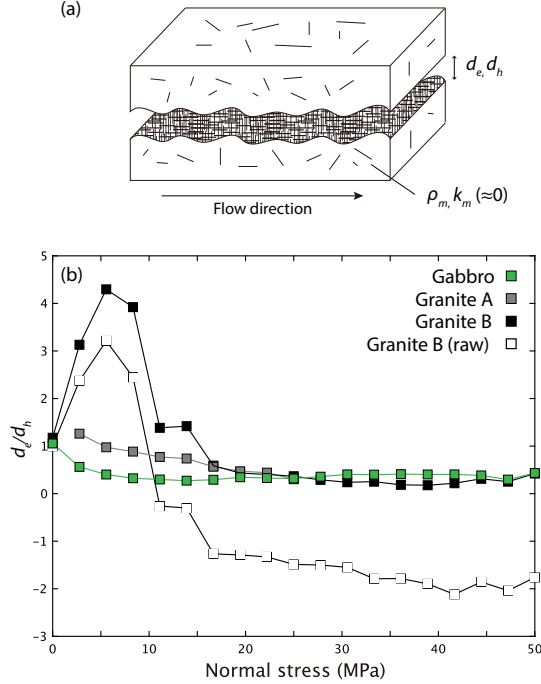
Fig. 9. (a) Schematics of the layered structure and (b) changes in electric-to-hydraulic aperture ratios as functions of normal stress.

le, similar to permeability. Meanwhile, resistivity in each sample diverged and approached their matrix values as stress increased. The discrepancies in the resistivity trends of the granite samples reflect their fracture aperture conditions: granite B has a smaller initial aperture value than granite A, resulting in the higher resistivity and lower permeability (Fig. 6). Similar to permeability, resistivity monotonically increased with stress in the gabbro sample but almost saturated at ~ 15 MPa in the granite samples. The hysteresis of resistivity was also consistent with the permeability trend, implying inelastic deformation during our hydromechanical loading process. Note that the resistivity in granite A at higher stress was missing due to the disconnection of the lead cable.

4. Discussion

4.1 Changes in permeability and resistivity due to aperture closure

Increasing normal stress decreased permeability and increased resistivity and stiffness in our experimental samples. Although the permeability and resistivity trends against stress were similar in different rock samples, the simple parallel-plate model exhibited a contrast in sensitivity between the cubic dependence of flow rate and linear dependence of electric current on the aperture (Brown, 1989). Fluid flow in a fracture is commonly described by the following cubic law:

$$Q = -\frac{W \langle d \rangle^3}{12\mu} \nabla P \tag{16}$$

where W is the fracture width and $\langle d \rangle$ is the mean aperture. In contrast, assuming that only an electrolyte carries electric

current in a single fracture, the associated electric current I is linearly related to $\langle d \rangle$ as (Brown, 1989):

$$I = -\frac{W \langle d \rangle}{\rho_f} \nabla V \tag{17}$$

where ∇V is the potential gradient. As stress increased, the mean aperture value continuously decreased, while permeability and resistivity exhibited saturation at high stress values (Figs. 5 and 8). This suggests that the mean aperture value does not completely explain the permeability and resistivity trends. Alternatively, we could evaluate the hydraulically or electrically effective aperture using Eqs. (16) or (17). Assuming negligible matrix permeability, the hydraulic aperture d_h could be expressed in terms of the flow rate during permeability measurement as:

$$d_h^3 = \frac{12\mu Q}{W \nabla P} \tag{18}$$

Meanwhile, matrix resistivity ρ_m exerted a non-negligible effect on the electric aperture d_e. The bulk resistance R_b of our experimental system (flow direction parallel to the layered structure; Fig. 9(a)) could be simply described as the harmonic average of fracture and matrix resistances, R_f and R_m:

$$\frac{1}{R_b} = \frac{1}{R_f} + \frac{1}{R_m} = \frac{A}{\rho_m} + \frac{W d_e}{\rho_f} \tag{19}$$

Eq. (19) could be simplified as:

$$d_e = \rho_f H \left(\frac{1}{\rho_b} - \frac{1}{\rho_m} \right) \tag{20}$$

where H is the sample height. Note that our experimental samples did not exhibit sufficiently high ρ_m, $\sim 10^3$ Ωm for granite and $\sim 10^4$ Ωm for the gabbro sample (Table 2).

Fig. 9(b) depicts the evolutions of the d_e/d_h ratios of the samples. The hydraulic and electric apertures of all samples were almost identical initially. The d_e/d_h ratio of the gabbro sample decreased with increasing stress. A previous numerical study also reported near-identical hydraulic and electric apertures when surfaces are widely separated, although d_e is always smaller than d_h; additionally, the difference between the two increases as the fracture closes (Brown, 1989). We verified that this trend was consistent with our results for the gabbro sample under the experimental hydromechanical loading process. However, the d_e/d_h ratio of granite increased during the early stage of loading. Because hydraulic paths were more tortuous than electric paths (Brown, 1989; Sawayama et al., 2021b), a higher value of d_e than d_h was unrealistic. The discrepancy in granite might be due to an increased matrix resistivity under initial loading, which closed microcracks (Katayama et al., 2023). An increase in the d_e/d_h ratio was followed by a decrease, indicating that matrix resistivity either recovers to its original state or further decreases. The increasing trend depended on the crack density of the matrix (Table 3). A further decrease in matrix resistivity yielded a negative electric aperture in the case of granite B. At crack initiation, matrix resistivity was halved from its original value (Katayama et al., 2023). By considering this effect, the
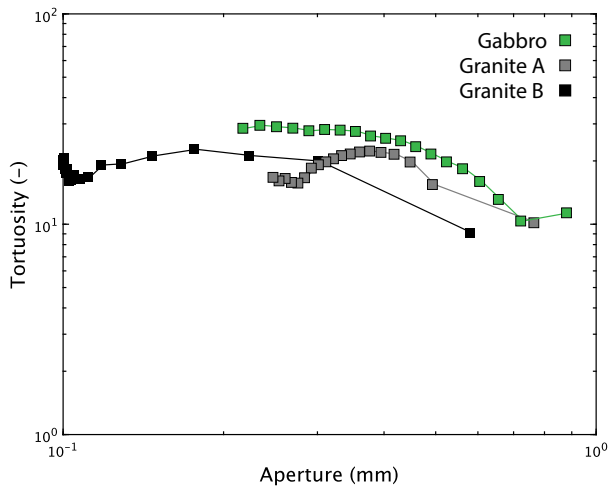
Fig. 10. Changes in tortuosity of gabbro (green) and granite (black and gray) as a function of aperture.

d_e/d_h ratio approached those of the other two samples. According to our data, the electric aperture was $0.3 - 0.4$ times the hydraulic aperture at normal stresses above 15 MPa, irrespective of the fracture surface roughness and rock type. Note that when quantifying the electric aperture of a granite sample, we must evaluate matrix resistivity during measurements, as suggested in our analysis.

The discrepancy between the electric and hydraulic apertures could be considered as a tortuosity difference between electrical and hydraulic flows. According to the equivalent channel model (Paterson, 1983; Walsh and Brace, 1984), permeability k could be written as functions of tortuosity τ^2 as follows:

$$k = \frac{\langle d \rangle^2 \phi}{12\tau^2} \qquad (21)$$

combining this equation with Eq. (16), we get $\tau^2 = \langle d \rangle / d_h$. Based on this formula, tortuosity was evaluated (Fig. 10). The calculated tortuosity increased with increasing fracture aperture closure (Fig. 10). This tortuosity increase was saturated at a certain point, which was also demonstrated in a previous numerical study (Sawayama et al., 2021b). Stagnant changes in tortuosity could be attributed to dominant flow paths becoming disconnected (Sawayama et al., 2023).

4.2 Cross-property relationship between permeability, resistivity, and stiffness in crystalline rocks

Having explored stress-induced permeability and resistivity changes, their respective relationships in crystalline rocks were further investigated. Overall, permeability is a nonlinear function of resistivity in logarithmic coordinates (Fig. 11(a)), indicating the universality of the nonlinear behavior observed in a numerical study that uses rough-walled fractures (Sawayama et al., 2023). Although a previous experimental study reported a linear correlation between the two parameters (Stesky, 1986), they used only two saw-cut fracture samples (Stesky, 1986). All of our experimental results using rough-walled fractures exhibit the nonlinear behavior, which suggests

that numerically proposed relationship between permeability and resistivity (Sawayama et al., 2023) can also be observed in the experimental rock deformation of naturally fractured crystalline rocks. This discrepancy between results possibly may arise from the rough surfaces of fractures, while saw-cut fractures can be assumed as parallel plates.

In detail, the permeability-resistivity relationships exhibited different trends in each sample. In the equivalent channel model, this relationship is expressed as a power law:

$$k \propto \rho^{-\alpha} \qquad (22)$$

where the slope α is theoretically related to the sensitivity of tortuosity to aperture closure (Fig. 10). As α increased, the tortuosity change became more sensitive to the aperture change (Brown, 1989). In granite, α decreased under high stress because tortuosity did not increase after the aperture was sufficiently closed (Fig. 10). In contrast, the tortuosity of the gabbro sample continuously increased with increasing aperture closure. Notably, this transition was absent in saw-cut samples (Stesky, 1986), indicating that it originated from the rough surface of the fracture. Based on Eq. (16), α is related to the d_e/d_h ratio ($\alpha = 3d_e/d_h$). The obtained d_e/d_h ratios was of $0.3 - 0.4$ under high stress, giving α a unity value. Meanwhile, when assuming the parallel-plate model or the saw-cut fracture (i.e., $d_e = d_h$), α became 3. Through a local flow-path analysis using granite fractures, Sawayama et al. (2023) demonstrated that α changes depend on flow path connection. The value of α becomes unity after dominant flow paths become disconnected, which is consistent with our experimental data under the high-stress condition. Therefore, the nonlinear trend might be related to substantial flow channeling, which is notable in rough-walled fractures. Although future study will elaborate on clarifying this trend with numerous datasets, the important point is that the trend should not be linear considering the hydromechanical deformation of naturally fractured crystalline rocks. Since a previous numerical study demonstrated that α does not depend on fracture surface roughness, fractal dimensions, shear displacement, and fracture size (Sawayama et al., 2021b, 2023), the variation of α may be related to the characteristics not fully modeled in the numerical calculation (e.g., matrix porosity and inelastic deformation).

The electric and hydraulic apertures were related to tortuosity, providing the physical meaning of α involving the d_e/d_h ratio. In a single fracture in an intact matrix having negligible permeability and electrical conductivity, α is bounded between 1 and 3 (Brown, 1989). However, the value of α exceeded 3 in some of our results. This tendency was also observed in a previous numerical study that considered a conductive matrix (Sawayama et al., 2024). The effects of the matrix on the hydraulic and electrical properties could be simply described as the harmonic average of the fracture and matrix resistances (Eq. (19)). The hydraulic resistances of a permeable matrix and fracture within a matrix are given by μ/kh and $12\mu/\langle d \rangle^3$, respectively. In the experimental setup with $\langle d \rangle = 1$ mm and $H = 30$ cm, matrix permeability was negligible ($< 10^{-19}$ m² for same lithology with our sample; Katayama et al., 2012; Sueyoshi et al., 2024), so
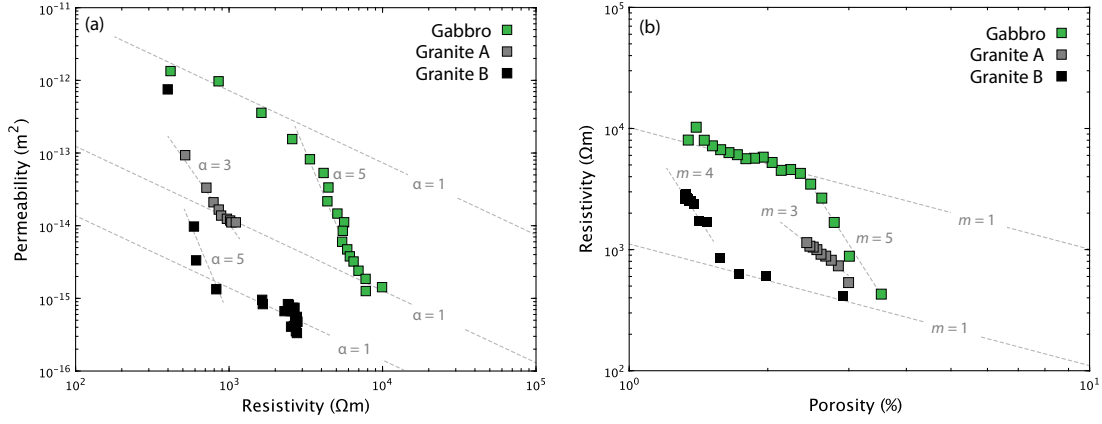
Fig. 11. Log-log correlations between (a) permeability-resistivity and (b) resistivity-porosity.

all changes in bulk permeability were attributed to fracture aperture closure. In contrast, our experimental sample did not exhibit sufficiently high resistivity, and matrix resistivity contributed to bulk resistivity (Eq. (16)), buffering a resistivity increase with aperture closure. The matrix effect was elicited primarily based on crack porosity (Table 2). As permeability was less sensitive to porosity than to resistivity, the slope α of the permeability-resistivity relationship increased with porosity (Sawayama et al., 2024). After the substantial crack closure (~ 15 MPa in our case), the de/dh ratios approached values of $0.3 - 0.4$. This implies that the matrix effect can be negligible in fractures in the deep subsurface that is deeper than ~ 550 m (assuming lithostatic stress in granite lithology), yielding $\alpha = \sim 1$. In electrical observations in EGS, resistivity changes were observed in approximately 5%-15% (Didana et al., 2017; Peacock et al., 2013; Johnson et al., 2024) after stimulating pre-existing fault systems. Based on our results, actual permeability changes were similar to or greater than the observed ranges of the resistivity change. The limitation of our study is the matrix porosity of the bed rock, where this study only examined low-porosity crystalline rocks. Although high-porosity rocks such as sandstone will have different trends with our results, the fractured granite of measured can be assumed to be analogous to geothermal reservoirs.

The inflection point of the permeability-resistivity relationship was independent of matrix permeability (Kirkby et al., 2016) but depended on matrix porosity (Sawayama et al., 2024). The nonlinearity of the permeability-resistivity relationship was also related to the non-Archie behavior. Empirically, resistivity and porosity follow a power-law relationship (Archie, 1942):

$$\rho = \rho_f \phi^{-m} \quad (23)$$

the Archie relations (log formation factor-log porosity plots) of our study samples were nonlinear, exhibiting a non-Archie behavior (Fig. 11(b)). Notably, the slope was higher than unity for granite under the low-porosity (i.e., high-stress) condition. Although the original Archie's equation is empirical, m will be physically dependent on the fractal dimension of the pore space in the case of porous media (Cai et al., 2017). Meanwhile, the equivalent channel model for resistivity case

can be described as:

$$\rho = \rho_f \tau^2 \phi^{-1} \quad (24)$$

combining Eqs. (23) and (24) gives:

$$m = 1 + \frac{\log \tau^2}{\log \phi} \quad (25)$$

This indicates that higher m values reflect more rapid changes in tortuosity with varying porosity. Hence, a higher m value of granite under the low-porosity condition may indicate the additional microcrack generation that increases tortuous flow paths. Through a local flow-path analysis using granite fractures, Sawayama et al. (2023) demonstrated $m = 1.2$ for the data of a fully connected flow regime but it increased for the data after dominant flow paths became disconnected. A lower m value represents higher α (Sawayama et al., 2023), which could also be seen in our datasets. In actual cracked rocks, porosity was $\sim 0.1 - 0.01$ (Heap and Kennedy, 2016) and fracture density (inverse of H) was ~ 10/m (Minato et al., 2017). The evolution of a damage zone depended on crustal steres and shear displacement (Mitchell and Faulkner, 2009).

At a shallow subsurface, the matrix effect would be considerable and porosity or permeability estimates based on electrical observations required further information. Accordingly, ths study obtained the permeability-stiffness relationship (Fig. 12(a)). Similar to the nonlinear permeability-resistivity relationship, the permeability-stiffness relationship exhibited an inflection point. A similar trend was observed for the permeability-stiffness relationship for two granite samples, although the absolute values were shifted, reflecting different fracture surface roughness conditions. However, the permeability-stiffness trend of the gabbro sample differed from that of granite. Based on a previous study, the permeability-stiffness relationship intrinsically depends on the fracture surface condition and Young's modulus of the host rock (Wang and Cardenas, 2016), which can be scaled with critical stiffness, defined as stiffness at the critical contact area (Petrovitch et al., 2013), where the substantial asperities are contacted. Although granite and gabbro showed no significant differences in their initial states, the stress sensitivity of each property differed between the samples. In addition, the observed per-
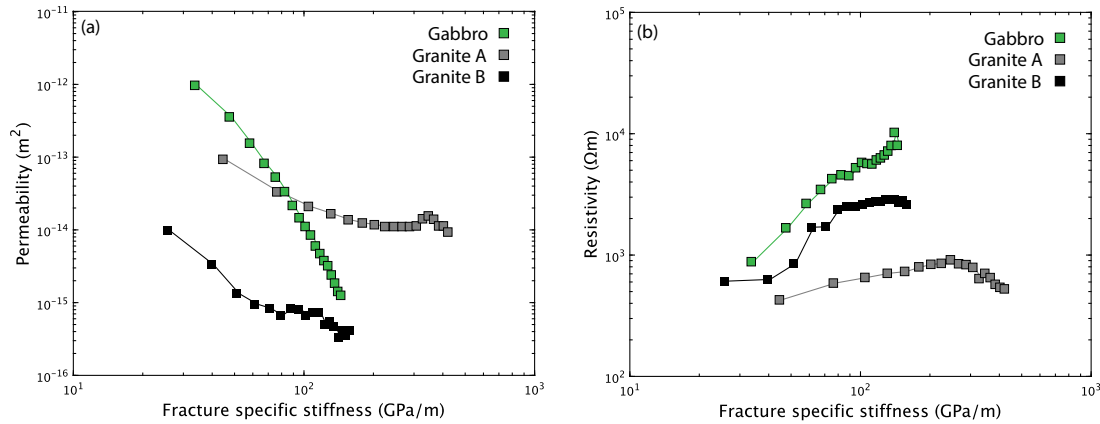
Fig. 12. Log-log correlations between (a) permeability-stiffness and (b) resistivity-stiffness.

meability hysteresis after loading differed between granite and gabbro. These results imply that the rock strength, which depends on the mineralogical composition of a rock, affects the degree of the inelastic behavior under hydromechanical loading. Meanwhile, a previous study demonstrated that the inelastic behavior changes the stress sensitivity of permeability owing to the evolution of flow-path tortuosity (Sawayama et al., 2021a). This tortuosity evolution progressively stagnates once the substantial area of asperity has been contacted under inelastic deformation. This study also observed varying trends in tortuosity changes between granite and gabbro (Fig. 10) (i.e., different mineralogical compositions), which may be related to their different cross-property relationships. Although a further study is needed to fully capture these effects, this integrated perspective based on a previous study and our new findings may suggest that the inconsistent cross-property relationships are relevant to inelastic behavior that varies with mineralogical compositions. Conversely, the resistivity-stiffness curves were similar for all rock types (Fig. 12(b)), possibly because unlike permeability, resistivity and stiffness are sensitive to the matrix, thereby canceling the effect of the matrix property. However, the resistivity-stiffness relationship varied with fracture surface roughness in rocks having the same lithology. Although the resistivity-stiffness relationship has not been previously reported and must be characterized through further study, our study demonstrated different sensitivities of the permeability-stiffness and resistivity-stiffness relationships. These different sensitivities of the resistivity, permeability, and stiffness properties suggest that simultaneously measuring the electrical and elastic properties is useful for interpreting permeability changes. Although further study is needed to fully elucidate the underlying physical mechanisms, our data can be a first report to experimentally observe the numerically proposed nonlinear behavior under the actual hydromechanical deformation of naturally fractured crystalline rocks.

5. Conclusions

The authors developed an experimental system that simultaneously measures permeability, electrical resistivity, and elastic property during uniaxial compression tests involving up to 50 MPa. Using this system, this study investigated the geophysical properties of fractured granite and gabbro with different values of fracture surface roughness and normal stress. Electrical resistivity and stiffness increased whereas permeability decreased with increasing normal stress. The electrical resistivity increase was lower in the granite samples than in the gabbro sample because granite has lower matrix resistivity than gabbro. The observed relationship between permeability and electrical resistivity in logarithmic coordinates was nonlinear. This result contradicts the linear results obtained previously using a saw-cut fracture sample; however, the relationship is consistent with a previous numerical study on rough-walled fractures. Based on the measured matrix properties, this study evaluated d_e and d_h and identified a decrease in their ratio (d_e/d_h) with increasing normal stress. After the closure of substantial cracks (at ~ 15 MPa in our case), the d_e/d_h ratio approached 0.3-0.4, implying that the matrix effect can be negligible in deep subsurface fractures. This implies that the actual permeability changes may be similar to or greater than those within the observed ranges of the resistivity change. In shallow subsurface where the matrix effect became significant, permeability estimates based on electrical observations required further information about the matrix property, which can be estimated based on the elastic property. The permeability-stiffness trend might be controlled primarily by the rock type, while the resistivity-stiffness trend depended on the fracture surface state. These different sensitivities exhibited by each property suggest that simultaneous measurements of the electrical and elastic properties can be advantageous for interpreting permeability changes. The developed experimental system can collect further datasets on changes in permeability, electrical resistivity, and fracture-specific stiffness while monitoring the stress and aperture change, which is not feasible in a previous study.

Conflict of interest

The authors declare no competing interest.

References

Akamatsu, Y., Hatakeyama, K., Katayama, I. Contrasting dilatant behaviors of mafic and ultramafic rocks based on triaxial deformation experiments. Journal of Mineralogical & Petrological Sciences, 2019, 114: 79-86.

Akamatsu, Y., Nagase, K., Abe, N., et al. Cross-property relationship between electrical resistivity and elastic wave velocity of crustal rocks from the Oman drilling project hole GT3A: Implications for in situ geophysical properties of oceanic crust. Journal of Geophysical Research: Solid Earth, 2023, 128: e2022JB026130.

Archie, G. E. The electrical resistivity log as an aid in determining some reservoir characteristics. Transactions of the AIME, 1942, 146: 54-62.

Brace, W. F. Permeability of crystalline and argillaceous rocks. International Journal of Rock Mechanics & Mining Sciences & Geomechanics Abstracts, 1980, 17: 241-251.

Brown, S. R. Transport of fluid and electric current through a single fracture. Journal of Geophysical Research: Solid Earth, 1989, 94: 9429-9438.

Cai, J., Wei, W., Hu, X., et al. Electrical conductivity models in saturated porous media: A review. Earth-Science Review, 2017, 171: 419-433.

Cai, J., Zhang, Z., Wei, W., et al. The critical factors for permeability-formation factor relation in reservoir rocks: Pore-throat ratio, tortuosity and connectivity. Energy, 2019, 188: 116051.

Didana, Y. L., Heinson, G., Thiel, S., Krieger, L. Magnetotelluric monitoring of permeability enhancement at enhanced geothermal system project. Geothermics, 2017, 66: 23-38.

Durham, W. B. Laboratory observations of the hydraulic behavior of a permeable fracture from 3800 m depth in the KTB pilot hole. Journal of Geophysical Research: Solid Earth, 1997, 102(B8): 18405-18416.

Fortin, J., Guéguen, Y., Schubnel, A. Effects of pore collapse and grain crushing on ultrasonic velocities andVp/Vs. Journal of Geophysical Research: Solid Earth, 2007, 112: B08207.

Glover, P. W., Zadjali, I. I., Frew, K. A. Permeability prediction from MICP and NMR data using an electrokinetic approach. Geophysics, 2006, 71: F49-F60.

Goodman, R. E. Methods of Geological Engineering in Discontinuous Rock. New York, USA, West Publishing Company, 1976.

Guéguen, Y., Dienes, J. Transport properties of rocks from statistics and percolation. Mathematical Geology, 1989, 21: 1-13.

Guéguen, Y., Palciauskas, V. Introduction to the Physics of Rocks. Princeton, UK, Princeton University Press, 1994.

Guéguen, Y., Sarout, J. Crack-induced anisotropy in crustal rocks: Predicted dry and fluid-saturated Thomsen's parameters. Physics of the Earth and Planetary Interiors, 2009, 172: 116-124.

Guyer, R. A., Johnson, P. A. Nonlinear mesoscopic elasticity: Evidence for a new class of materials. Physics Today, 1999, 52: 30-36.

Heap, M. J., Kennedy, B. M. Exploring the scale-dependent permeability of fractured andesite. Earth & Planetary Science Letters, 2016, 447: 139-150.

Hofmann, H., Blöcher, G., Milsch, H., et al. Transmissivity of aligned and displaced tensile fractures in granitic rocks during cyclic loading. International Journal of Rock Mechanics & Mining Sciences, 2016, 87: 69-84.

Johnson, T. C., Burghardt, J., Strickland, C., et al. 4D electrical resistivity imaging of stress perturbations induced during high-pressure shear stimulation tests. Geophysical Research Letters, 2024, 51: e2024GL108423.

Kachanov, M. Elastic solids with many cracks and related problems, in Advances in Applied Mechanics Volume 30, edited by J. W. Hutchinson and T. Y. Wu, Elsevier, Amsterdam, pp. 259-445, 1993.

Katayama, I., Aoi, Y., Tanimoto, K., et al. Simultaneous electrical resistivity and elastic wave velocity measurements during triaxial deformation of granite under brine-saturated conditions. Earth, Planets & Space, 2023, 75: 56.

Katayama. I., Terada, T., Okazaki, K., et al. Episodic tremor and slow slip potentially linked to permeability contrasts at the Moho. Nature Geoscience, 2012, 5(10): 731-734.

Kirkby, A., Heinson, G., Krieger, L. Relating permeability and electrical resistivity in fractures using random resistor network models. Journal of Geophysical Research: Solid Earth, 2016, 121: 1546-1564.

Liu, Y., Xue, Z., Park, H., et al. Measurement of electrical impedance of a Berea sandstone core during the displacement of saturated brine by oil and CO_2 injections. Journal of Applied Geophysics, 2015, 123: 50-62.

Matsuki, K., Chida, Y., Sakaguchi, K., et al. Size effect on aperture and permeability of a fracture as estimated in large synthetic fractures. International Journal of Rock Mechanics & Mining Sciences, 2006, 43: 726-755.

Matsunaga, Y., Kanda, W. Numerical modeling of a volcanic hydrothermal system based on resistivity structure. Journal of Disaster Research, 2022, 17: 654-662.

Minato, S., Ghose, R., Tsuji, T., et al. Hydraulic properties of closely spaced dipping open fractures intersecting a fluid-filled borehole derived from tube wave generation and scattering. Journal of Geophysical Research: Solid Earth, 2017, 122: 8003-8020.

Mitchell, T. M., Faulkner, D. R. The nature and origin of off-fault damage surrounding strike-slip fault zones with a

wide range of displacements: A field study from the Atacama fault system, northern Chile. Journal of Structural Geology, 2009, 31: 802-816.

Nara, Y., Meredith, P. G., Yoneda, T., et al. Influence of macro-fractures and micro-fractures on permeability and elastic wave velocities in basalt at elevated pressure. Tectonophysics, 2011, 503(1-2): 52-59.

Nolte, D. D., Pyrak-Nolte, L. J., Cook, N. G. W. The fractal geometry of flow paths in natural fractures in rock and the approach to percolation. Pure & Applied Geophysics, 1989, 131: 111-138.

O'Connell, R. J., Budiansky, B. Seismic velocities in dry and saturated cracked solids. Journal of Geophysical Research, 1974, 79: 5412-5426.

Park, S. K. Monitoring resistivity changes prior to earthquakes in Parkfield, California, with telluric arrays. Journal of Geophysical Research: Solid Earth, 1991, 96: 14211-14237.

Paterson, M. S. The equivalent channel model for permeability and resistivity in fluid-saturated rock-A re-appraisal. Mechanics of Materials, 1983, 2(4): 345-352.

Peacock, J. R., Thiel, S., Heinson, G. S., et al. Time-lapse magnetotelluric monitoring of an enhanced geothermal system. Geophysics, 2013, 78: B121-B130.

Petrovitch, C. L., Nolte, D. D., Pyrak-Nolte, L. J. Scaling of fluid flow versus fracture stiffness. Geophysical Research Letters, 2013, 40: 2076-2080.

Pyrak-Nolte, L. J., Morris, J. P. Single fractures under normal stress: The relation between fracture specific stiffness and fluid flow. International Journal of Rock Mechanics & Mining Sciences, 2000, 37: 245-262.

Pyrak-Nolte, L. J., Cook, N. G. W., Nolte, D. D. Fluid percolation through single fractures. Geophysical Research Letters, 1988, 15: 1247-1250.

Raven, K. G., Gale, J. E. Water flow in a natural rock fracture as a function of stress and sample size. International Journal of Rock Mechanics & Mining Sciences & Geomechanics Abstracts, 1985, 22: 251-261.

Sawayama, K., Ishibashi, T., Jiang, F., et al. Relating hydraulic-electrical-elastic properties of natural rock fractures at elevated stress and associated transient changes of fracture flow. Rock Mechanics & Rock Engineering, 2021a, 54: 2145-2164.

Sawayama, K., Ishibashi, T., Jiang, F., et al. Scale-independent relationship between permeability and resistivity in mated fractures with natural rough surfaces. Geothermics, 2021b, 94: 102065.

Sawayama, K., Ishibashi, T., Jiang, F., et al. Relationship between permeability and resistivity of sheared rock fractures: The role of tortuosity and flow path percolation. Geophysical Research Letters, 2023, 50, e2023GL104418.

Sawayama, K., Ishibashi, T., Jiang, F., et al. Hydro-mechanical-electrical simulations of synthetic faults in two orthogonal directions with shear-induced anisotropy. Journal of Rock Mechanics & Geotechnical Engineering, 2024, 16: 4428-4439.

Stesky, R. M. Electrical conductivity of brine-saturated fractured rock. Geophysics, 1986, 51: 1585-1593.

Sueyoshi, K., Katayama, I., Sawayama, K. Permeability evolution in fine-grained Aji granite during triaxial compression experiments. Geophysical Prospecting, 2024, 72: 675-684.

Tsang, Y. W., Witherspoon, P. A. Hydromechanical behavior of a deformable rock fracture subject to normal stress. Journal of Geophysical Research: Solid Earth, 1981, 86: 9287-9298.

Walsh, J. B., Brace, W. F. The effect of pressure on porosity and the transport properties of rock. Journal of Geophysical Research: Solid Earth, 1984, 89(B11): 9425-9431.

Wang, L., Cardenas, M. B. Development of an empirical model relating permeability and specific stiffness for rough fractures from numerical deformation experiments. Journal of Geophysical Research: Solid Earth, 2016, 121: 4977-4989.

Watanabe, T., Higuchi, A. Simultaneous measurements of elastic wave velocities and electrical conductivity in a brine-saturated granitic rock under confining pressures and their implication for interpretation of geophysical observations. Progress in Earth & Planetary Science, 2015, 2: 37.

Xue, L., Li, H. B., Brodsky, E. E., et al. Continuous permeability measurements record healing inside the Wenchuan earthquake fault zone. Science, 2013, 340(6140): 1555-1559.

Yamaya, Y., Suzuki, Y., Murata, Y., et al. 3-D resistivity imaging of the supercritical geothermal system in the Sengan geothermal region, NE Japan. Geothermics, 2022, 103: 102412.

Yasuhara, H., Elsworth, D., Polak, A. Evolution of permeability in a natural fracture: Significant role of pressure solution. Journal of Geophysical Research: Solid Earth, 2004, 109: B03204.